Title

Subtitle

by

Mikkel Metzsch Jensen

THESIS

for the degree of

MASTER OF SCIENCE

Faculty of Mathematics and Natural Sciences
University of Oslo

Spring 2023

Title

Subtitle

Mikkel Metzsch Jensen

Title

http://www.duo.uio.no/

Printed: Reprosentralen, University of Oslo

Abstract

Abstract.

Acknowledgments

Acknowledgments.

Contents

List of symbols?

Maybe add list of symbols and where they are used like Trømborg.

Chapter 1

Background Theory and Method

Small introtext to motivate this chapter. What am I going to go over here.

1.1 Tribology - friction

1.1.1 Friction on a macroscopic scale - macroscale theories

1.1.1.1 Amontons' law.

The work of Leonardo da Vinci (1452–1519), Guillaume Amontons (1663-705) and Charles de Coulomb (1736-1806) all contributed to what is commonly known as Amontons' law describing the frictional force accuring when starting and keeping a solid block sliding against a solid surface. This emperical law states that the frictional force tangential to the sliding direction is entirely independent of contact area and sliding velocity (at ordinary sliding velocities). Instead it relies only on the normal force F_N acting from the surface on the block and the material specific friction coefficient μ as

$$F_f = \mu F_N.$$

Further it distinguish between *static* and *kinetic* friction as the cases of stationary and sliding contact resepectively. Each type of friction comes with its own friction coefficient, μ_s for static and μ_k for kinetic friction, usually with values lower than one and $\mu_s \geq \mu_k$ in all cases. [1][p. 6].

This simple law is a natural starting point for the

Allthough this model is a common base for understanding friction on a macroscopic level is has its limitations. It turns out that static friction is not constant, but depends on the so-called contact history with increasing friction as the logarithm of time of stationary contact [2]. For the kinetic friction the independency of sliding velocity dissapears at low velocities as thermal effects becomes important and for high velocities due to intertial effetcs. [1][pp. 5-6].

It fails to explain the mechanisms behind fritction.

In order to understand what is causing friction between moving objects and how this might result in a linear relationship between friction and normal force we must take the study to a smaller scale... Having an emperical law that seems to predict the friction in many cases leads to the next natural desire for deriving these from fundamental atomic or molecular principles.

1.1.2 Friction on a microscopic scale - Nanotribology

It is generally accepted that friction is caused by two mechanism: mechanical friction and chemical friction. The mechanical friction is the plowing of the surface by hard particles or asperities. The chemical mechanism is adhesion between contacting surfaces. [3].

Sources in general: [4], [3]

1.1.2.1 Surface roughness - Asperity theories

Going beyond a macroscopic perspective we realise that most surfaces is in fact rough. The contact between two surfaces consist of numerous smaller contact point, so-called asperities, each with a contact area of A_{asp}. The true contact area $\sum A_{\text{asp}}$ is found to be much smaller than the apperent macroscopic area A_{macro}. The friction force is shown to be proportional (extra source on this) to this true contact area as

$$F_f = \tau \sum A_{\text{asp}},$$

where τ is an effective shear strength of the contacting bodies. This is still compatible with Amontons' law as long as we differenciate between the macroscopic macroscopic and true area and by having the true contact area dependt linearly on applied normal force.

Thus many studies have focused individual asperities to reveal the relationship between the contact area and normal force (13-15 from [4]). By assuming perfectly smooth asperities with radii of curvature from nanometers to micrometres in size continuum mechanics can be used to predict the deformation of asperities as normal force is applied. A model for non-adhesive contact between homogenous, isotropic, linear elastic spheres was first developed by Hertz (17 [4]), which predicted $A_{\text{asp}} \propto F_N^{2/3}$. Later adhesion effects were included in a number of subsequent models, including Maugis-Dugdale theory (18 from [4]), which also predicts a sublinear relatinship between A_{asp} and f_N leading to a similar sublinear relationship for F_f and F_N.
[4].

1.1.2.2 Atomic level friction

On the smallest possible scale, atomic scale, the surfaces does not have structural asperities. Instead atomic level friction is being model as a consequencse of the rough potential of the atomic landscape.

1.1.2.3 Frenkel-Kontorova-Tomlinson (FKT)

Describes atomic scale friction (not fully accurately though) and gives insight in stick slip motion.

1.1.2.4 Commensurate and incommensurate

1.1.2.5 Stick slip

At nanoscales things get a bit more unclear. SFM (explain) experiments have reported (copy sources 5, 6, 21 from [4]) where $F_f \propto F_N$ or even with these quantities being nearly independent of each other.

In several works by J. Fineberg's group [2–4] the transition from sticking to sliding is characterized by slip fronts propagating along the interface. [5][p. 2].

1.1.2.6 Commensurate and incommensurate

As expected, high levels of friction were present in the commensurate positions and extremely low friction was found when the surfaces were incommensurate. (https://physicsworld.com/a/friction-at-the-nano-scale/)

1.1.2.7 Superlubricity?

Superlubricity, now a pervasive concept of modern tribology, dates back to the math- ematical framework of the Frenkel Kontorova model for incommensurate interfaces [40]. When two contacting crystalline workpieces are out of registry, by lattice mismatch or angular misalignment, the minimal force required to achieve sliding, i.e. the static friction, tends to zero in the thermodynamic limit – that is, it can at most grow as a power less than one of the area – provided the two substrates are stiff enough. (Current trends in the physics of nanoscale friction)

Superlubricity is experimentally rare. Until recently, it has been demonstrated or im- plied in a relatively small number of cases [29, 42–46]. There are now more evidences of superlubric behavior in cluster nanomanipulation [32, 33, 47], sliding colloidal layers [48–50], and inertially driven rare-gas adsorbates [51, 52]. (Current trends in the physics of nanoscale friction)

A breakdown of structural lubricity may occur at the heterogeneous interface of graphene and h-BN. Because of lattice mismatch (1.8%), this interface is intrinsically incommen- surate, and superlubricity should persist regardless of the flake-substrate orientation, and become more and more evident as the flake size increases [57]. However, vertical cor- rugations and planar strains may occur at the interface even in the presence of weak van der Waals interactions and, since the lattice mismatch is small, the system can de- velop locally commensurate and incommensurate domains as a function of the misfit angle [58, 59]. Nonetheless, spontaneous rotation of large graphene flakes on h-BN is observed after thermal annealing at elevated temperatures, indicative of very low friction due to incommensurate sliding [60, 61]. (Current trends in the physics of nanoscale friction)

Indeed, we know from theory and simulation [74–76] that even in clean wearless friction experiments with perfect atomic structures, superlubricity at large scales may, for example, surrender due to the soft elastic strain deformations of contacting systems. (Current trends in the physics of nanoscale friction)

1.1.3 Temperature dependence

Thus, it is commonly expected that the friction of a dry nanocontact should classically decrease with increasing temperature provided no other surface or material parameters are altered by the temperature changes [77, 80–83]. (Current trends in the physics of nanoscale friction)

1.1.4 Summary of expected frictional properties

1. Friction should decrease by increasing temperature.
2. We expect stick slip motion
3. What about dependence on normal force?
4. Dependence on contact area?
5. Dependense on speed?

- Different friction models on macro-and microscopic scale

1.1.5 Graphene friction

Theory of friction experiment involving graphene.

Because of this frictional reduction, many studies indicate graphene as the thinnest solid-state lubricant and anti-wear coating [104–106]. (Current trends in the physics of nanoscale friction)

Accurate FFM measurements on few-layer graphene systems show that friction decreases by increasing graphene thickness from a single layer up to 4-5 layers, and then it approaches graphite values [97, 99, 101, 107, 108]. (Current trends in the physics of nanoscale friction)

1.2 Molecular Dynamics

- MD simulation (classical or ab initio)
- Basics of classical MD simulations: Integration and stuff
- Ab initio simulation (quantum mechanics, solving schrödinger)

1.2.1 Potentials

The choices of potentials used in the MD simulation is mainly based on the on [6] which have a somewhat similar MD friction simulation, the difference being that they impose a Si-tip on the graphene sheet supported by a Si-substrate where we impose drag the whole sheet upon the substrate. Nonetheless this serves as a good anchor for the methodology of the setup. The covalent bonds of C-C in graphene and Si-Si in the substrate is described by the Tersoff and Stillinger–Weber potentials, respectively. A typical 12-6 Lennard–Jones potential is used to describe the van der Waals adhesive interaction between graphene and the substrate.

1.2.1.1 General formulation of potentials...?

On a general note we can generalize the n-body potential as the expansion in orders of participating atoms as

$$E = \sum_i V_1(\mathbf{r}_i) + \sum_{\substack{i,j \\ i<j}} V_2(\mathbf{r}_i, \mathbf{r}_j) + \sum_{i,j,k \atop i<j<k} V_3(\mathbf{r}_i, \mathbf{r}_j, \mathbf{r}_i) + \cdots .$$

where $\mathbf{r}_n$ is the position of the nth particle and V_m is called an m-body potential [7]. The first one-body term corresponds to an external potential, followed by the two-body term, the three-body term and so on.The simplest model that includes parrticle interaction is the pair potential truncating the expansion after the two-body term. A general feature of the pair potentials is that they favor close-packed structures which is unsuited to describe covalent bonds that take more open structures. In particular, pair potentials are completely inapplicable to strongly co- valent systems such as semiconductors [7]. In order to accomodate the description of covalent bonds the natural step is thus to include the next step of the expansion, the three-body terms, as we will see for the modeling of the graphene sheet C-C bonds and the Silicon sheet Si-Si bonds. For the interaction between the sheet and the substrate we can nøjes med a Lennard Jones pair potential describing the non-bonded van der Waals interaction.

1.2.2 Lennard Jones

This sections is based on [[8], [9], [10]].

The Lennard-Jones (LJ) model is probably one of the most famous pair potentials used in MD simulations. LJ models the potential energy between two non-bonding atoms based solely on interatomc distance r. The model accounts for attractive forces arising from dipole-dipole, dipole-induced dipole and London interactions, and repulsive forces that capture the hard core (is this safe to say?) of overlapping wave functions at small distances. Thus it is assummes neutrally charged atoms and was orginally proposed for noble gases. The classical 12-6 version of the model (refering to the power law of the repulsive and attractive forces respectively) reads

$$E = 4\epsilon \left[\left(\frac{\sigma}{r}\right)^{12} - \left(\frac{\sigma}{r}\right)^{6} \right], \qquad r < r_c, \tag{1.1}$$

where r is the interatomic distance with cut-off r_c, ϵ is the depth of the potential well and σ the distance where the potential is zero. By solving for the potential minimum ($dE/dr = 0$) we find the equilibrium distance to be $r_0 = \sigma 2^{1/6}$. This makes for an even cleary interpration of σ which effectively sets the equilirbium distance between atoms, i.e. the dividing line for which the net force is repulsive or attractive. While the LJ model in many ways is an oversimplified model that is insufficient in its description of ... (get source and concrete examples) it is commonly used as a model for intermaterial interactions (between moving object and substrate) in friction studies [[6], [11], [3]].

1.2.3 Stillinger weber

This section is based on [[12], [13]]

The stillinger weber potential takes the form of a three body potential

$$E = \sum_i \sum_{j>i} \phi_2(r_{ij}) + \sum_i \sum_{j\neq i} \sum_{k>j} \phi_3(r_{ij}, r_{ik}, \theta_{ijk}),$$

where r_{ij} denotes the distance between atom i and j and θ_{ijk} the angle between bond ij and jk. The summations is over all neighbours j and k of atom i within a cut-off distance $r = a\sigma$.
The two-body term ϕ_2 builds from the LJ model with the addition of an exponetial cutoff term

$$\phi_2(r_{ij}) = A_{ij}\epsilon_{ij}\left[B_{ij}\left(\frac{\sigma_{ij}}{r_{ij}}\right)^{p_{ij}} - \left(\frac{\sigma_{ij}}{r_{ij}}\right)^{q_{ij}}\right]\exp(\frac{\sigma_{ij}}{r_{ij} - a_{ij}\sigma_{ij}}). \tag{1.2}$$

The model parameters A, ϵ, B, σ, p, q and a comes with i, j indices to indicate that theese parameters should be specified for each unique pair of atom types. However, in our case we will only provide a single value for each model parameter as we are exclusively dealing with Si-Si bonds. We see that the first term in eq. (1.2) is reminiscent of the LJ model in eq. (1.1) while the last term effectively drives the potential to zero at $r = a\sigma$, which is thus the chosen cut-off distance for the potential evaluation. With the model parameters for the Si-Si modelling (see table 1.1) the cut-off becomes ~ 3.8 Å.
The three body term includes an angle dependency as

$$\phi_3(r_{ij}, r_{ik}, \theta_{ijk}) = \lambda_{ijk}\ \epsilon_{ijk}\Big[\cos\theta_{ijk} - \cos\theta_{0,ijk}\Big]^2 \exp(\frac{\gamma_{ij}\sigma_{ij}}{r_{ij} - a_{ij}\sigma_{ij}})\exp(\frac{\gamma_{ik}\sigma_{ik}}{r_{ik} - a_{ik}\sigma_{ik}}), \tag{1.3}$$

where $\theta_{0,ijk}$ is the equilibrium angle. The first term of eq. (1.3) includes an angle dependency analog to a harmonic oscillator based on a cosine angle distance from the equilibrium angle. The final two terms act again as a cut-off function by driving the potential to zero at $r_{ij} = a_{ij}\sigma_{ij}$ and $r_{ik} = a_{ik}\sigma_{ik}$ respectively.
The parameters used for the Si-Si bond modeling is displayed in table 1.1 along with an interpretation of each model parameter.

Table 1.1: Parameters for the stilliner weber potential used for intermolecular interactions in the silicon substrate.

Parameter	Value	Description
ϵ	2.1683	Individual depth of the potential well for each atom type pair/tiplets.
σ	2.0951	Distance for which the individual pair interactions has zero potential (analog to the LJ model).
a	1.80	The individual cut-off distance for each atom type pair.
λ	21.0	The overall depth of the three-body potential well.
γ	1.20	The shape of the three-body cut-off terms.
$\cos(\theta_0)$	-1/3	Cosine of equilibrium angle.
A	7.049556277	The overall depth of the two-body potential well.
B	0.6022245584	Scales the repulsion part of the two-body term.
p	4.0	The power dependency for the repulsion part of the two-body term.
q	0.0	The power dependency for the attraction part of the two-body term.
tol	0.0	LAMMPS: Option to define a different cut-off than the theoretical of $r = a\sigma$. $tol = 0$ refers to the theoretical being used.

1.2.4 Tersoff

This section is based on [[14], [7]].

The tersoff potential abandon the idea of a general n-body form and attempts instead to build the model on a more physics informed approach; The more neighbours an atom has the weaker the bonds will be. Thus it introduces the bond order (bond strentgh), that is environment specific and decrease with increasing bond coordination (number of neighbours for a given atom). The potential energy is taken to have the form

$$E = \sum_i E_i = \frac{1}{2}\sum_{i\neq j} V_{ij},$$
$$V_{ij} = f_C(r_{ij})\big[f_R(r_{ij}) + b_{ij}f_A(r_{ij})\big],$$

where the total potential energy is decomposed into a bond energy V_{ij}. The indices i and j run over the atoms of the system with r_{ij} denoting the distance between atom i and j. Notice that the sum includes all combinations of i, j where $i \neq j$ meaning that the same bond is double counted which is the reason for the additional factor 1/2. The reasoning behind comes from the asymmetry of the bond order $b_{ij} \neq b_{ji}$ leading to a $V_{ij} \neq V_{ji}$. The bond energy is composed of a repulsive term f_R, arising from overlapping wave functions, and an attractive term f_A associated with bonding. f_c is simply a smooth cut-off function to increase computational efficiency. b_{ij} represent the bond order, i.e. the strength of the bonds, which depends inversely on the number of bonds, the bond angles (θ_{ijk}) and optionally the relative bonds lengths (r_{ij}, rjk). Notice that an additional cut-off term a_{ij} was orginally multiplied to f_R as a way of including terms that limit the range of the interactions to the first neighbour shell. These kind of limitations is already included in b_{ij} for the attractive term f_A but is often omitted for the repulsive term f_R, and we do so to by setting $a_{ij} = 1$.
The cut-off function f_C goes from 1 to 0 over a small interval range $R \pm D$ as

$$f_C(r) = \begin{cases} 1 & r < R - D \\ \frac{1}{2} - \frac{1}{2}\sin\left(\frac{\pi}{2}\frac{r-R}{D}\right) & R - D < r < R + D \\ 0 & r > R + D \end{cases},$$

which is continuous and differentiable for all r. R is usually chosen to include only the first neighbour shell.
The repulsive and attractive terms f_R and f_A is modelled as an exponetial function, similar to a morse potential,

$$f_R(r) = A\exp(-\lambda_1 r),$$
$$f_A(r) = -B\exp\big(-\lambda_2 r\big).$$

The novel feature of the model lies in modeling of the bond order b_{ij} which includes three-body interactions by summing over a third atom $k \neq i, j$ within the cut-off $r_{ik} < R + D$ as shown in the following.

$$b_{ij} = \left(1 + \beta^n \zeta_{ij}^n\right)^{-\frac{1}{2n}} \tag{1.4}$$

$$\zeta_{ij} = \sum_{k \neq i,j} f_C(r_{ik}) g\Big(\theta_{ijk}\left(r_{ij}, r_{ik}\right)\Big) \exp\left({\lambda_3}^m \big(r_{ij} - r_{ik}\big)^m\right) \tag{1.5}$$

$$g(\theta) = \gamma_{ijk}\left(1 + \frac{c^2}{d^2} - \frac{c^2}{\left[d^2 + (\cos\theta - \cos\theta_0)^2\right]}\right). \tag{1.6}$$

In eq. (1.6) $\zeta_{i,j}$ is an effective coordination and $g(\theta)$ captures angle dependency as it is minimized at the equilibrium angle $\theta = \theta_0$.
The parameters used to model the graphene C-C bonds is summarized in table 1.2

Table 1.2: Parameters for the tersoff potential used for intermolecular interations in the graphene sheet

Parameter	Value	Description
m	3.0	Default (not used since $\lambda_3 = 0$)
γ	1.0	...
λ_3	0.0 Å^{-1}	...
c	3.8049×10^4	Strength of the angular effect
d	4.3484	Determines the "sharpness" of the angular dependency
$\cos(\theta_0)$	-0.57058	Cosine of the equilibrium angle
n	0.72751	Power law exponent for the bond order dependency
β	1.5724×10^{-7}	...
λ_2	2.2119 Å^{-1}	Decay of repulsion potential term
B	346.74 eV	Attractive potential term minimum at core ($r_{ij} = 0$).
R	1.95 Å	Center distance for cut-off
D	0.15 Å	Thickness of cut-off layers
λ_1	3.4879 Å^{-1}	Decay of repulsion potential term
A	1393.6 eV	Repulsion potential term at core ($r_{ij} = 0$)

1.2.5 LAMMPS

1.2.6 Integration

Having defined a system of particles governed by interartomic potentials we need to move the system forward in time. By solving newtons equations of motion we sample the microcanonical ensemble characterized by a constant number of particles N, volume V and energy E, hence denoted NVE. Newtons equaiton of motion read

$$m_i \frac{d^2\mathbf{r}_i}{dt^2} = \mathbf{F}_i = -\nabla U_i \tag{1.7}$$

where i is the particle index and m_i its mass, $\mathbf{r}_i = (x_i, y_i, z_i)$ the position, t is time, $\nabla_i = (\frac{\partial}{\partial x_i}, \frac{\partial}{\partial y_i}, \frac{\partial}{\partial z_i})$ and U_i the potential energy. In our case the potential energy is a function of the particle positional configuration of nearby particles depending on the specefic potential in use. Since the forces defined by the potentials is conservative the energy should be conserved when solving the equations defined by eq. (1.7). We recognize that the second order partial differential equations can be split into two coupled first order differential equations as

$$\dot{\mathbf{v}}_i(t) = \frac{\mathbf{F}}{m_i}, \qquad \dot{\mathbf{r}}_i(t) = \mathbf{v}_i(t), \tag{1.8}$$

where $\dot{x} = dx/dt$ (Newton's notation) and $\mathbf{v} = (v_x, v_y, v_z)$ is velocity.

Numerically we can solve the coupled equations (eq.(1.8)) by integrating a temporal discretization of the problem. That is, we discretize the time $t_k = t_0 + k \cdot \Delta t$ with timestep Δt and integrate to compute t_{k+1}.

1.2.6.1 Velocity Verlet

A common algorithm to integrate Newtons equation of motion (eq.(1.8)) is the velocity verlet. We can derive the algorithm by the use of Taylor exopansions. We begin by expanding the next-step position vector $\mathbf{r}_i(t + \Delta t)$ at time t

$$\mathbf{r}_i(t + \Delta t) = \mathbf{r}_i(t) + \dot{\mathbf{r}}_i(t)\Delta t + \frac{\ddot{\mathbf{r}}_i(t)}{2}\Delta t^2 + \mathcal{O}(\Delta t^3), \tag{1.9}$$

where $\ddot{\mathbf{r}} = d^2\mathbf{r}/dt^2$ and Δt^n is just the relaxed notation for to $(\Delta t)^n$. Similar we take the expansions of the next-step velocity vector $\mathbf{v}_i(t + \Delta t)$ at time t

$$\mathbf{v}_i(t + \Delta t) = \mathbf{v}_i(t) + \dot{\mathbf{v}}_i(t)\Delta t + \frac{\ddot{\mathbf{v}}_i(t)}{2}\Delta t^2 + \mathcal{O}(\Delta t^3). \tag{1.10}$$

By taking the expansion of $\dot{\mathbf{v}}_i(t + \Delta t)$ we can eliminate the $\ddot{\mathbf{v}}_i$ term in eq. (1.10) as done in the following.

$$\begin{aligned}
\dot{\mathbf{v}}_i(t + \Delta t) &= \dot{\mathbf{v}}_i(t) + \ddot{\mathbf{v}}_i(t)\Delta t + \mathcal{O}(\Delta t^2) \\
\frac{\ddot{\mathbf{v}}_i(t)}{2}\Delta t^2 &= \frac{\Delta t}{2}\Big(\dot{\mathbf{v}}(t + \Delta t) - \dot{\mathbf{v}}_i(t)\Big) + \mathcal{O}(\Delta t^3) \\
&\Downarrow \\
\mathbf{v}_i(t + \Delta t) &= \mathbf{v}_i(t) + \dot{\mathbf{v}}_i(t)\Delta t + \frac{\Delta t}{2}\Big(\dot{\mathbf{v}}_i(t + \Delta t) - \dot{\mathbf{v}}_i(t)\Big) + \mathcal{O}(\Delta t^3) \\
&= \mathbf{v}_i(t) + \frac{\Delta t}{2}\Big(\dot{\mathbf{v}}_i(t) + \dot{\mathbf{v}}_i(t + \Delta t)\Big) + \mathcal{O}(\Delta t^3).
\end{aligned} \tag{1.11}$$

By combining eq. (1.9) and eq. (1.11) and using Newton's second equation $\dot{\mathbf{v}} = \mathbf{F}_i(t)/m_i =$ and $\mathbf{v} = \dot{\mathbf{r}}$ we arrive at the final scheme. One of the most popular ways to implement the scheme numerially is as stated in the following steps.

1. Calculate $v_{k+\frac{1}{2}} = v_k + \frac{F_k}{2m}\Delta t$.
2. Calculate $r_{k+1} = r_k + v_{k+\frac{1}{2}}\Delta t$.
3. Evaluate the force $F_{k+1} = F(r_{k+1})$.
4. Calculate $v_{k+1} = v_{k+\frac{1}{2}} + \frac{F_{k+1}}{2m}\Delta t$

1.2.7 Thermostats

Langevin thermostat

When solving newtons equations of motion as in REF we are modelling the microcanonical ensemble defined by the constants: number of particles N, system volume V and internal energy E. Hence the microcanonical ensemble is often denoted NVE. The canonical ensemble is achieved by keeping temperature T constant in exchange for the energy being free to change. This is theoretically defined as a finite system in contact with an infinte heat bath of temperature T. In equilibrium the finite system of interest will have reached the same temperature. In order to specify the temperature of our system we introduce a so-called thermostat transistioning from NVE to NVT. By doing so we essentially modidy newtons equations of motion such that the equilibrium solution is a part of the canonical ensemble

The NVT ensemble is equivalent to sampling a system en theromodynamic equilibrium where the weight of each microscopic state is given by the boltzmann factor $\exp[-E/(k_B T)]$.

The Langevin equation is the modified version of Newtons second law for a Brownian particle. A brownian particle is a small particle suspendend in liquid, e.g. pollen or dust, named after Robert brown (1773–1858) which was the first to observe its jittery motion. The langevin equation describes these dynamics by the combination of viscous drag force $-\gamma\mathbf{v}$, where γ is a positive friction coefficient and $\mathbf{v}$ the velocity vector, and a random fluctuation force $\mathbf{R}$. The langevin equation reads

$$m\frac{d\mathbf{v}}{dt} = -\gamma\mathbf{v} + \mathbf{R} \tag{1.12}$$

where m is the particle mass. This effectively describes the particle of interest, the brownian particle, as being suspendend in a sea of smaller particles. The collision with these smaller particles is modelled by the drag force and the fluctuation force. We notice that if the fluctuation force is excluded eq. (1.12) becomes

$$m\frac{d\mathbf{v}}{dt} = -\gamma\mathbf{v} \quad \Rightarrow \quad \mathbf{v}_i(t) = v(0)e^{-\frac{\gamma t}{m}},$$

where the solution predicts that brownian particle will come to a complete stop after a long time $\mathbf{v}_i(t \to \infty) \to \mathbf{0}$. This is in violation with the equipartion theorem

$$\frac{1}{2}m\langle v^2\rangle_{eq} = \frac{k_B T}{2}.$$

The fluctuation force is hence nessecary to obtain the correct equilibrium.

We do the following calculations in one dimension in order to simplify the notation. We describe the statistical nature of the collisions as a sum of independent momentum transfers

$$\Delta P = \sum_i^N \delta p_i$$

where ΔP denotes the change of momentum after N momentum momentum transfers δp_i to the brownian particle. We assume the first and second moments $\langle \delta p\rangle = 0$ and $\langle \delta p\rangle = \sigma^2$. When N is large the central limit theorem states that the random variable ΔP has a gaussian distribution with $\langle P\rangle = 0$ and $\langle \Delta P^2\rangle = N\sigma^2$. If ΔP is the momentum change over a discrete time Δt, where the number of collisiosn is proportional to time $N \propto \Delta t$, the corresponding fluctuation force $\Delta R = \Delta P/\Delta t$ will have a variance

$$\langle R^2\rangle = \frac{\langle \Delta P^2\rangle}{\Delta t^2} = \frac{N\sigma^2}{\Delta t^2} \propto \frac{1}{\Delta t}.$$

In a computer simulation we need to pick a random force $R(t)$ from a Gaussian distribution every time-step Δt. These forces will not be correlated as long as Δt is larger than the correlation time of the forces from the

molecules which we will assume for this model (I think there exist corrections for this to refer to here). With this assumption we can write the correlation function as

$$\langle R(t)R(0)\rangle = \begin{cases} \frac{a}{\Delta t}, & |\Delta t| < \Delta t/2 \\ 0, & |\Delta t| > \Delta t/2, \end{cases}$$

where a is some strength of (...?). In the limit $\Delta t \to 0$ the correlation function becomes

$$\langle R(t)R(0)\rangle = a\delta(t), \tag{1.13}$$

where δ denotes the dirac delta function. This is valid for all spatial coordinates which will all be independent of each other. Since both the drag force and the fluctuation force originate from the molecular fluid, where the drag force $-\alpha\mathbf{v}$ is velocity dependent it is reasonible to assume that fluctuation force is independent of velocity $\langle R_i v_j\rangle$ for all cartesian indices i and j.

From the Langevin equation eq. (1.12) we can compute the velocity autocorrelation function. We do this in one dimension for simplicity. We multiply by $(e^{\gamma t/m})/m$

$$\dot{v}(t)e^{\gamma t/m} + \frac{\gamma}{m}v(t)e^{\frac{\gamma t}{m}} = \frac{F}{m}e^{\frac{\gamma t}{m}},$$

and integrate from $t = -\infty$. By the use of integration by parts on latter term in the left hand side we calculate the velocity

$$\begin{aligned} \int_{-\infty}^{t} dt'\ \dot{v}(t')e^{\frac{\gamma t'}{m}} + \frac{\gamma}{m}v(t)e^{\frac{\gamma t'}{m}} &= \int_{-\infty}^{t} dt'\ e^{\frac{\gamma t'}{m}}\frac{F(t')}{m} \\ \int_{-\infty}^{t} dt'\ \dot{v}(t')e^{\frac{\gamma t'}{m}} + \left(\left[v(t')e^{\frac{\gamma t'}{m}}\right]_{-\infty}^{t} - \int_{-\infty}^{t} dt'\ \dot{v}(t')e^{\frac{\gamma t'}{m}}\right) &= \int_{-\infty}^{t} dt'\ e^{\frac{\gamma t'}{m}}\frac{F(t')}{m} \\ v(t) &= \int_{-\infty}^{t} dt'\ e^{\frac{-\gamma(t-t')}{m}}\frac{F(t')}{m}, \end{aligned}$$

where $e^{\frac{-\gamma t}{m}}$ plays the role of a response function (?). We can then calculate the autocorrelation

$$\begin{aligned} \big\langle v(t)v(0)\big\rangle &= \int_{-\infty}^{t} dt_1 \int_{-\infty}^{0} dt_2\ e^{\frac{t-t_1-t_2}{m}}\frac{\langle F(t_1)F(t_2)\rangle}{m^2} \\ &= \int_{-\infty}^{t} dt_1 \int_{-\infty}^{0} dt_2\ e^{\frac{t-t_1-t_2}{m}}\frac{a\delta(t_1-t_2)}{m^2} \\ &= \int_{-\infty}^{0} dt_2\ e^{\frac{t-2t_2}{m}}\frac{a}{m^2} = \frac{a}{2m\gamma}e^{-\frac{\gamma t}{m}} \end{aligned}$$

where we used eq. (1.13) and that the integration commutes with the average (we can change the order of integration). By comparing this with the equipartition theorem we get

$$\begin{aligned} \frac{1}{2}m\langle v^2\rangle &= \frac{k_B T}{2} \\ \frac{1}{2}m\langle v(0)v(0)\rangle &= \frac{k_B T}{2} \\ \frac{a}{4\gamma} &= \frac{k_B T}{2} \\ a &= 2\gamma k_B T \end{aligned}$$

We notice the appereance of γ meaning that the magnitude of the fluctuations increase both with friction and temperature. Further we can integrate the velocity over time to get displacement $x(t)$ and show that the variance

$$\langle x^2(t) \rangle = \frac{2kT}{\gamma} t$$

which represents the einstein relation with $D = kT/\gamma$ where $\gamma = 1/\mu$

This section is based on [15], [16](pp. 115, 120-121) and [17]

"The Langevin equation is Newtons second law for a Brownian particle, where the forces include both the viscous drag due to the surrounding fluid and the fluctuations caused by the individual collisions with the fluid molecules."

"Another option to simulate a system in the NVT ensemble is to use a stochastic thermostat, as opposed to the deterministic thermostat defined through the Nose-Hoover equations."

"The equations of mo- tion of a system with a stochastic thermostat are known as Brownian dynamic equations"

In order to simulate the canonical ensemble, that is the ensemble defined by a constant amount of particles N, constant temperature T and constant volume V, hence often denoted NVT, we apply a so-called thermostat. There exist a variety of such including Nosé-Hoover, Gaussian, Berendsen, Langevin thermostat and many other (give example of how they modify) We will use the ladder.
The connical ensemble is an ensemble of systems by the assumption that the system of interests is connected to an infitely large heat bath of temperature T. The Langevin thermostat assumes that the particles collides with much smaller lighter particles representing the heat bath as a sea of small particles. The collisions is described by a friction force $f_f = -\gamma \mathbf{p}$, where γ is positiv friction coefficient and $\mathbf{p}$ the momentum vector, and a random force $f_r = \mathbf{R}_i(t)$. By denoting the conservative force arising from the usual inter-particle interactions $\mathbf{f}_i$ on particle i we get the Langevin equations of motion describing the total force $\mathbf{F}_i$ on particle i as

$$\begin{aligned} \mathbf{F}_i &= \mathbf{f}_i + \mathbf{f}_{f,i} + \mathbf{f}_{r,i} \\ m_i \ddot{\mathbf{r}}_i &= \mathbf{f}_i - \gamma_i \mathbf{p}_i + \mathbf{R}_i(t) \end{aligned} \tag{1.14}$$

where m_i is the mass of particle i $\mathbf{r}_i$ the position vector. The random force $\mathbf{R}_i(t)$ is described as gaussian white noise and have the following properties.

1. It is uncorrelated with the velocities $\dot{\mathbf{r}}(t)$ and deterministic forces $\mathbf{f}_i(t')$ at previous times $t' < t$.
2. The time average is zero: $\langle \mathbf{R}(t) \rangle = \mathbf{0}$.
3. The mean-square components evaluate to $2m_i\gamma_i k_B T$.
4. The force component of particle i $R_{i,\mu}$ along cartesian axis μ is uncorrelated with any component of particle j $R_{i,\nu}$ along cartesian axis ν, unless $i = j$, $\mu = \nu$ and $t = t'$.

The ladder two conditions can be formulated as

$$\langle R_{i,\mu}(t) R_{j,\nu}(t') \rangle = 2m_i\gamma_i k_B T \delta_{ij} \delta_{\mu\nu} \delta(t' - t),$$

where $\delta_{..}$ is the Kronecker Delta function and $\delta(\cdot)$ is the Dirac Delta function. It can be shown that a trajectory generated by integrating the Langevin equations of motion (eq. (1.14)) maps a cononical distribution of microstates at temperature T. [16](p.121). (Can I say something more about the relationship between the friction froce and the random force - How to the balance to give NVT. Is the proof complicated?)

In practice the implementation of the thermostat is implemented discretely by updating the force on each particle by the addition of the described forces f_f and f_r for each particle. In LAMMPS this is controlled by the user defined damping factor "damp" $= \gamma^{-1}$ in units of time whih control how fast we are going to reach the temperature equlibrium. Thus the documentation ([17]) defines the added forces as

$$f_f = -\frac{m}{\text{damp}}, \qquad f_r \propto \sqrt{\frac{mk_BT}{dt\ \text{damp}}}$$

where $v = \dot{[}r]$ is the velocity. The definition of f_f falls straight out of the definition above in eq. (1.12) while the proportionality of f_r comes from

$$\sqrt{\langle R(t)^2 \rangle} = \sqrt{2m\gamma k_B T} \propto \sqrt{\frac{mk_B T}{\text{damp}}}$$

Thus we have $f_r \propto \sqrt{\langle R(t)^2 \rangle / dt}$ which I do not quite understand. It is mentioned in https://pubs.acs.org/doi/full/10.1021/ct8002173 when talkikng about residual forces, as it is natural when taking a step length of dt... Probably simply, but check this later.

1.3 Defining the system

1.3.1 Groups: Sheet, pullblocks and substrate

Include figure of system to point out thermo layers and freeze layers.

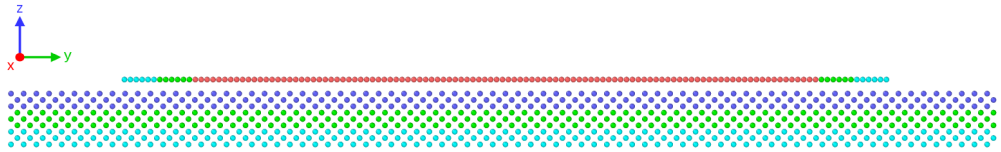

(a) Side view

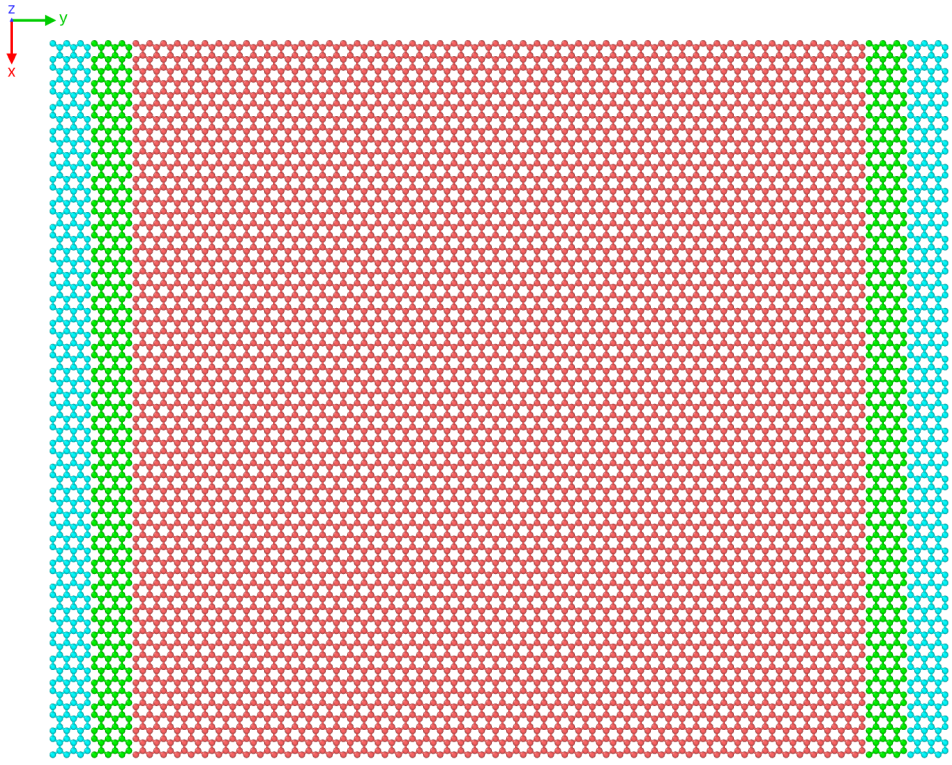

(b) Top view

Figure 1.1: System. 27456 atoms in total: 7272 with thermostat (orange), 7272 is locked (light blue) and the remaing 12912 just with NVE. (Get better colors)

Table 1.3: System atom count and region division.

Region	**Total**	Sub region	Sub total	**NVE**	**NVT**	**Locked**
Sheet	7800	Inner sheet	6360	6360	0	0
		Pull blocks	1440	0	720	720
Substrate	19656	Upper	6552	6552	0	0
		Middle	6552	0	6552	0
		Bottom	6552	0	0	6552
All	27456			12912	7272	7272

1.3.2 Creating sheets

We are going to create a 2D sheet graphene sheet.

1.3.2.1 Graphene

Graphene is a single layer of carbon atom, graphite is the bulk, arranged in a hexagonallattice structure. We can describe the 2D crystal structure in terms of its primitive lattice vector and a basis. That is we populate each lattice site by the given basis and translate it to fill the whole plane by any linear combination of the lattice vectors

$$\mathbf{T}_{mn} = m\mathbf{a_1} + n\mathbf{a_2}, \qquad m, n \in \mathbb{N}.$$

For graphene we have the primitive lattice vectors

$$\mathbf{a_1} = a\left(\frac{\sqrt{3}}{2}, -\frac{1}{2}\right), \qquad \mathbf{a_2} = a\left(\frac{\sqrt{3}}{2}, \frac{1}{2}\right), \qquad |\mathbf{a_1}| = |\mathbf{a_2} = 2.46 \text{ Å}.$$

Notice that we deliberately excluded the third coordinate as we only consider a single graphene layer on not the bulk graphite consisting of multiple layers stacked on top of each other. The basis is

$$\left\{\Big(0,0\Big), \frac{a}{2}\Big(\frac{1}{\sqrt{3}}, 1\Big)\right\}$$

It turns out that the spacing between atoms is equal for all paris with an interatomic distance

$$\left|\frac{a}{2}\Big(\frac{1}{\sqrt{3}}, 1\Big)\right| \approx 1.42 \text{ Å}.$$

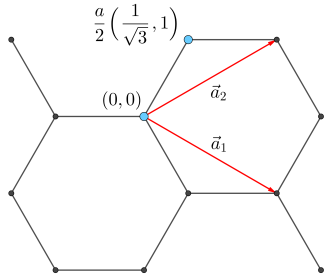

Figure 1.2: Graphene crystal structure with basis.

1.3.2.2 Indexing

In order to define the cut patterns applied to the graphene sheet we must define an indexing system. We must ensure that this gives an unique description of the atoms as we eventually want to pass a binary matrix, containg 0 for removed atom and 1 for present atom, that uniquely describes the sheet. We do this by letting the x-coordinate point to zigzag chains and the y-coordinate to the position along that chain. This is illustrated in figure 1.3. Other solutions might naturally invole the lattice vectors, but as these only can be used to translate to similar basis atoms a unfortunate duality is introduced as ones need to include the basis atom of choice into the indexing system. With the current system we notice that locallity is somewhat preserved. That is, atom (i, j) is in the proximity of $\{(i+1, j), (i-1, j), (i, j+1), (i, j-1)\}$, but only three of them is categorized as nearest neighbours due to the hexgonal structure of the lattice. While $(i, j \pm 1)$ is always nearest neighbours the neighbour in the x-direction flip sides with incrementing y-coordinate. That is the nearest neighbours (NN) is decided as

$$j \text{ is even} \rightarrow \text{NN} = \{(i+1, j), (i, j+1), (i, j-1)\},$$
$$j \text{ is odd} \rightarrow \text{NN} = \{(i-1, j), (i, j+1), (i, j-1)\}.$$

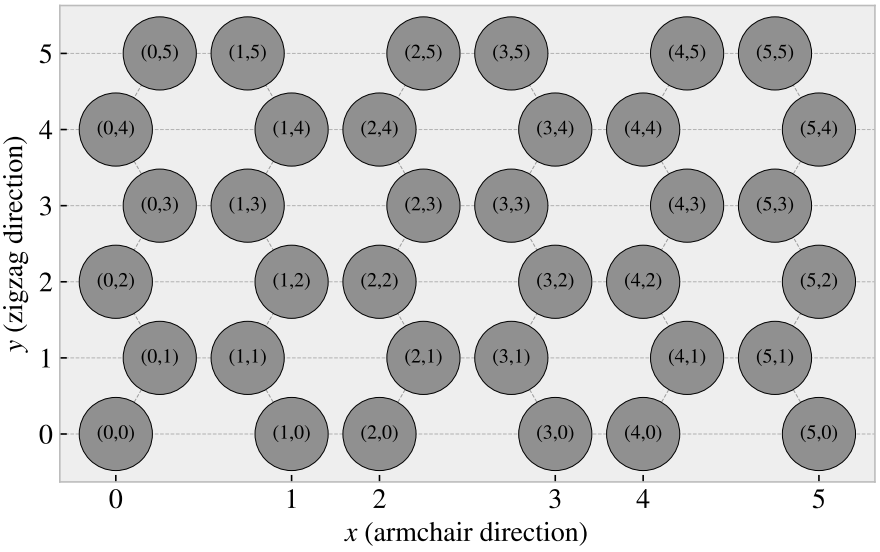

Figure 1.3: Graphene atom indexing

1.3.2.3 Removing atoms

As a mean to ease the formulation of cut patterns we introduce pseudo center element in each gap of the hexagonal honeycombs, see figure 1.4.

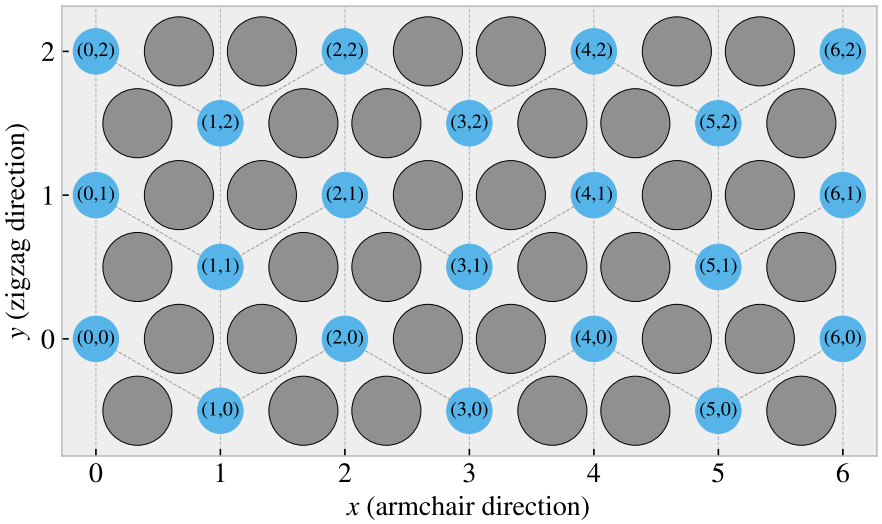

Figure 1.4: Graphene center indexing

Similar to the case of the indexing for the carbon atoms themself the nearest neighbour center elements alternate with position, this time along the x-coordinate. Each center element has six nearest neighbours, in clock wise direction we can denote them: "up", "upper right", "lower right", "down", "lower left", "upper left". The "up" and "down" is always accesed as $(i, j \pm 1)$, but for even i the $(i+1, j)$ index corresponds to the "lower right" neighbour while for odd i this corresponds to the "upper right" neighbour. This shifting applies for all left or right neighbours and the full neighbour list is illustrated in figure 1.5.

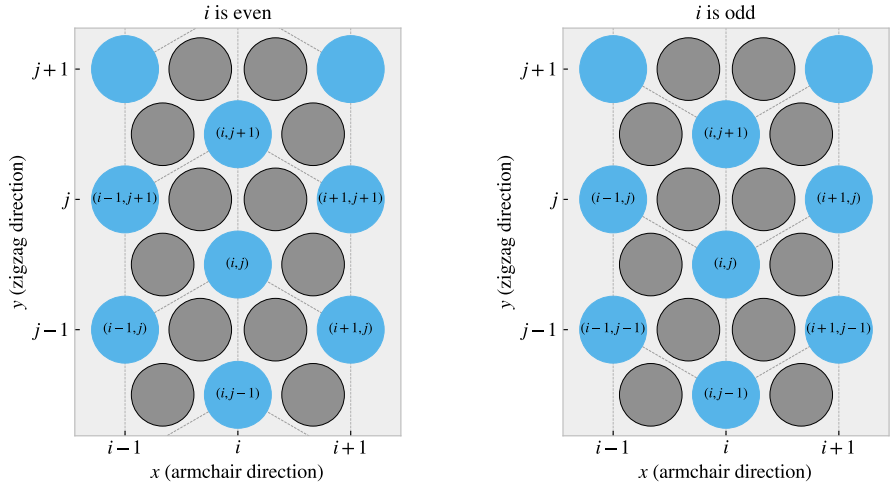

Figure 1.5: Graphene center elements directions

We define a cut pattern by connecting center elements into connected paths. As we walk element to element we remove atoms according to one of two rules

1. Remove intersection atoms: We remove the pair of atoms placed directly in the path we are walking. That is, when jumnping to the "up" center element we remove the two upper atoms located in the local hexagon of atoms. This method is sensitive to the order of the center elements in the path.

2. Remove all surrounding atoms: We simply remove all atoms in the local hexagon surrounding each center element. This method is indepdent of the ordering of center elements in the path.

We notice that removing atoms using either of these rules will not garuantee an unique cut pattern. Rule 1 is the more sensitive to paths but we realize that, for an even i, we will remove the same five atoms following

either of the following paths.

$$(i,j) \to \underbrace{(i+1,j+1)}_{\text{upper right}} \to \underbrace{(i,j+1)}_{\text{up}} \to \underbrace{(i+1,j+2)}_{\text{upperright + up}} \to \underbrace{(i+1,j+1)}_{\text{upper right}}$$
$$(i,j) \to \underbrace{(i+1,j+1)}_{\text{upper right}} \to \underbrace{(i+1,j+2)}_{\text{upperright + up}} \to \underbrace{(i,j+1)}_{\text{up}}$$

For rule 2 it is even more abovious that different paths can result in the same atoms being removed. This is the reason that we needed to define and indexing system for the atom position itself even though that all cuts generated manually will use the center element path as reference.

Illustrate some delete path?

1.3.3 Pull blocks

1.3.4 Kirigami inspired cut out patterns

1.3.4.1 Pop-up pattern

1.3.4.2 Honeycomb

1.3.4.3 Random walk

1.4 Fourier Transform (light)

Find out where to put this if nessecary.

Fourier transform is a technique where we transform a function $f(t)$ of time to a function $F(k)$ of frequency. The Forward Fourier Transform is done as

$$F(k) = \int_{-\infty}^{\infty} f(t) e^{-2\pi i k x} dx$$

For any complex function $F(k)$ we can decompose it into magnitude $A(k)$ and phase $\phi(k)$

$$F(k) = A(k) e^{i\phi(k)}$$

Hence when performing a Forward Fourier transform on a time series we can determine the amplitude and phase as a function of freqeuncy as

$$A(k) = |F(k)|^2, \qquad \phi(k) = \Im \ln F(k)$$

1.4.1 Real life experimental procedures

From Introduction to Tribology, Second Edition, p. 526:

The surface force apparatus (SFA), the scanning tunneling microscopes (STM), and atomic force and friction force microscopes (AFM and FFM) are widely used in nanotribological and nanomechanics studies.

- Real life procedures to mimic in computation, for instance Atomic Force Microscoopy (AFM) for friction measurements.
- Available technology for test of my findings if successful (possibilities for making the nano machine)

1.5 Machine Learning (ML)

- Feed forward fully connected
- CNN
- GAN (encoder + decoder)
- Genetic algorithm
- Using machine learning for inverse designs partly eliminate the black box problem. When a design is produced we can test it, and if it works we not rely on machine learning connections to verify it's relevance.
- However, using explanaitons techniques such as maybe t-SNE, Deep dream, LRP, Shapley values and linearizations, we can try to understand why the AI chose as it did. This can lead to an increased understanding of each design feature. Again this is not dependent on the complex network of the network as this can be tested and veriied independently of the network.

1.5.1 Feed forward network / Neural networks

1.5.2 CNN for image recognition

1.5.3 GAN (encoder + deoder)

1.5.4 Inverse desing using machine learning

1.5.5 Prediction explanation

1.5.5.1 Shapley

1.5.5.2 Lineariations

1.5.5.3 LRP

1.5.5.4 t-SNE

Simulations

Frictional properties of the intact graphene sheet

The friction measurment simulation is governed by the following parameters, which is divided into three sub categories for the purpose of this thesis as shown in table 1.4.

Table 1.4: Parameters of the numerical procedure for measuring friction.

Category	Parameter name: description	Category purpose
Physical	- T: Temperature for the Langevin thermostat. - v_{drag}: Drag speed for the sheet translation.	Parameters that we expect to have an inevitably effect on the system friction properties, for which the choice will be a baseline for our studies.
Measurement	- dt: Integration timestep. - t_R: Relaxtion time before strething. - Pauses between stretch and adding normal force and between dragging the sheet. - Stretch Speed: How fast to stretch the sheet. - K: Spring constant for the spring responsible of translating the sheet. An infinte spring constant is achieved by moving the end blocks as a rigid body (Lammps: fix move). - Drag Length: How far to translate the sheet. - Sheet size: Spatial size of the 2D sheet.	Paramters that effects the simulation dynamics and the 'experimental procedure' that we a mimicking. We aim to choose to these paramters such that the friction properties is stable for small perturbations.
ML input	- Sheet configuration: A binary matrix containing information of which atoms is removed (0) and which is still present (1) in the graphene structure. - Scan angle: The direction for which we translate the sheet. - Stretch amount: The relative sheet stretch in percentage. - F_N: Applied normal force to the end blocks.	The ramaining paramters that serve as the governing variables in the optimization process for certain friction properties and is thus the input variables for the ML part.

We should try to set the physcis and measurement parameters in such a way that we reduce computation speed where it is doesn't infer with the frictional properties study.

We need to define some ranges for the ML input paramters. F_N, stretch ranges where it is not prone to ruptures. The configuration it self does not have clear rules but is also being regulated by the no rupture requirement.

1.5.6 Baseline

1.5.6.1 Single measurement

Force oscillations We first assess the raw data for the friction force $F_{\parallel}$ parallel to the drag direction as seen in figure 1.6. The sample rate is 10 ps^{-1} for which we sample the the mean of all previous timesteps. We observe that the data carriers oscillations on different time scales. By applying a savgol filter to data with a polyorder of 5 and window length corresponding to a drag length of 3.0 Å (or time interval 15.0 ps) we can qualitatively point out at least two different frequencies of osccilation. On figure 1.6a we see roughly three waves on the savgol filter corresponding to one frequency, while on 1.6b the same savgol filter reveals an even slower frequency on top of the first creating a visual patterns of a wavepacket.

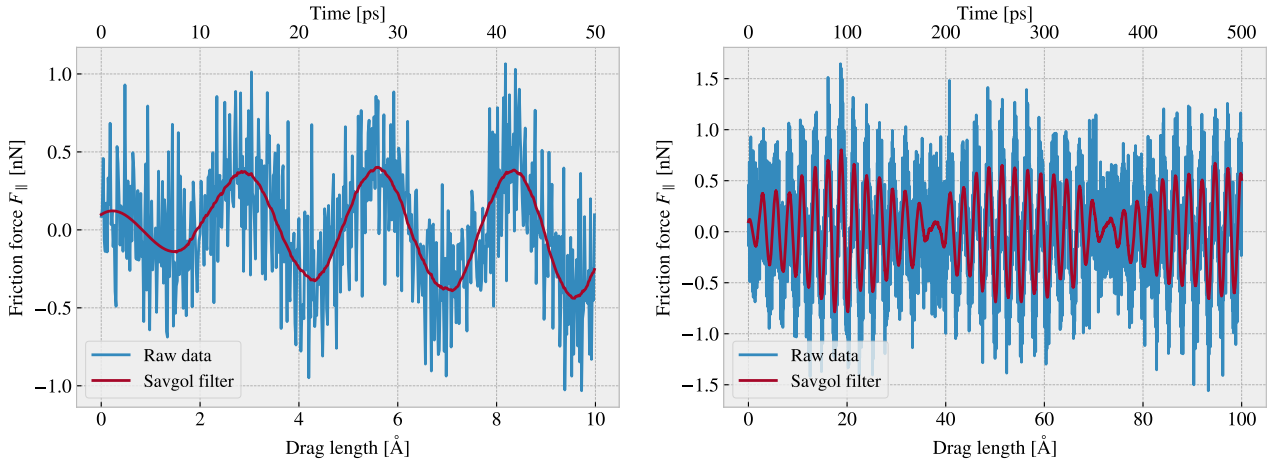

(a) Drag length of 10 Å.

(b) Drag length of 100 Å.

Figure 1.6: Friction force $F_{\parallel}$ between (full) sheet and substrate with respect to the drag direction vs. drag length. The drag length is measured by the constant movement of the virtual atom and not the COM of the sheet. The red line represents a savgol filter with window polyorder 5 and windoew length 150 (corresponding to a drag length of 3 Å or a time window of 15 ps)

By performing a Forward Fourier Transform of the data (using FFT) we can quantitavely idendity some of the leading frequencies as seen in figure 1.7a. By plotting the two most dominant frequencies $f_1 = 0.0074$ ps $^{-1}$ and $f_2 = 0.0079$ ps $^{-1}$ as $\sin(2\pi f_1) + \sin(2\pi f_2)$ we find a convincing fit to the observed wavepacket shape as seen in figure 1.7b. By using the trigonometric identity

$$\sin(\alpha+\beta) = \sin(\alpha)\cos(\beta) + \cos(\alpha)\sin(\beta),$$
$$\sin(\alpha-\beta) = \sin(\alpha)\cos(\beta) - \cos(\alpha)\sin(\beta),$$

and decomposing $f_1 = a - b$, $f_2 = a + b$ we can rewrite the sine sum as the sinusoidal product

$$\begin{aligned}\sin(2\pi f_1)\sin(2\pi f_2) &= \sin(2\pi(a-b))\sin(2\pi(a+b)) \\ &= \sin(a)\cos(b) + \cancel{\cos(2\pi a)\sin(2\pi b)} + \sin(2\pi a)\cos(2\pi b) - \cancel{\cos(2\pi a)\sin(2\pi b)} \\ &= 2\sin(2\pi a)\cos(2\pi b),\end{aligned}$$

with

$$a = \frac{f_1+f_2}{2} = 0.0763 \pm 0.0005\text{ps}^{-1}, \qquad b = \frac{f_2-f_1}{2} = 0.0028 \pm 0.0005\text{ps}^{-1},$$
$$= 0.381 \pm 0.003\text{Å}^{-1}, \qquad = 0.014 \pm 0.003\text{Å}^{-1},$$

where the latter frequency is denoted with respect to drag length. This makes us recognize the fast osccilation frequency as a and the slower frequency as b. We also take note of the longest period in the data $T_b = 1/b \sim 357$ ps ~ 71 Å^{-1} which will be relevant for the evaluation of measurement incertainty.

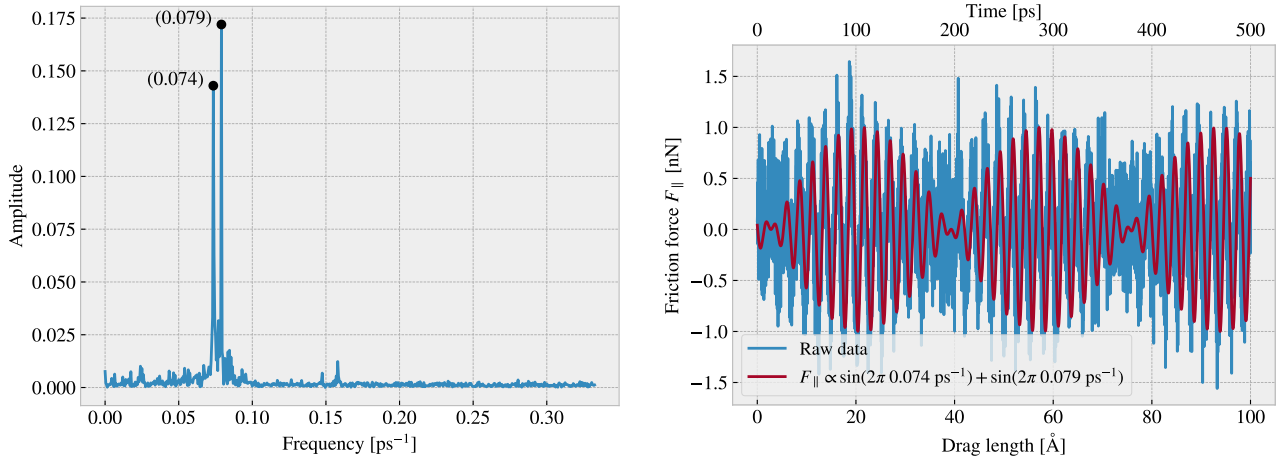

(a) Reduced frequency range.

(b) Selected frequencies applied to data from figure 1.6b

Figure 1.7: Fourier transform on data shown in figure 1.6.

Decompositions In the previous analysis we have looked only as the friction force for the full sheet, including the pullblocks which is locked off during the drag, and with respect to the drag direction.

Since we are only applying cuts to the inner sheet (excluding the pull blocks), it might seem more natural to only consider the friction on that part. If the desired frictional properties can be observed from the inner sheet we can always scale the relative size between inner sheet and pull block. However, when looking at the time series of friction force decomposed onto inner sheet and pull block (figure 1.8a) we observe the friction force arrising from those parts is seemingly antisymmetric. That is, the fricitonal pull on the substrate is oscillating between the inner sheet and the pullblock. Remembering that the normal forc eis only applied to the pull block we might take this as an integrated feature of the system. An interesting nonlinear friction coefficient might depend on this internal distribution of forces. Hence we hedge our bets an use the full sheet friction force.

Similar we might question the decision of only considering the frictional force projected on the direction of the drag as we are neglecting the "side shift" induced during the drag phase. In figure 1.8b we see the decomposition into force components parallel $F_\parallel$ and perpendicular $F_\perp$ to the drag direction respectively. We see that the most dominant trends is projected into the parallel component. If we want to include the perpendicular component as well we would have to evaluate the friction as the length of the vector for which we loose the sign of direction. Hence we would only get positive contributions, meaning a resisting force, which is not faithfully capturing the sheet oscillaitons that make the friction forces act both against in with the direction of drag. By this argument we decide to use only the parallel component going forward.

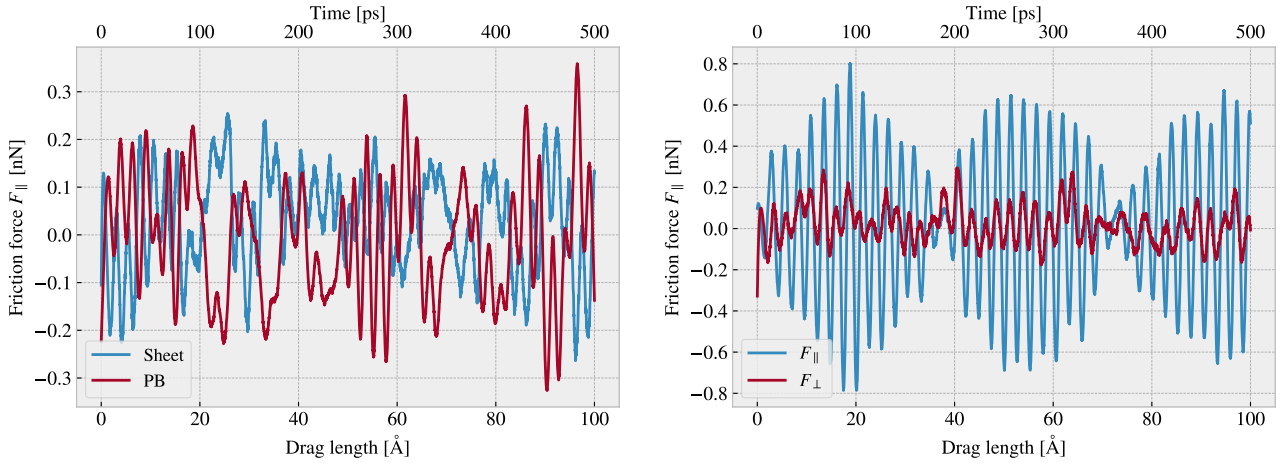

(a) Decomposition into group inner sheet (sheet) and pull blocks (PB).

(b) Decomposition into parallel (∥) and perpendicular (⊥) to drag direction.

Figure 1.8: Decomposition into parallel (∥) and perpendicular (⊥) to drag direction showing the savgol filter applied

Center of mass path From the previous observations we already have evidence of a stick slip behaviour, judging from the friction oscillations in figure 1.6, and motion partial motion perpendicular to the drag direction, judging from the perpendicular force component in figure 1.8b. By looking at the x, y-position for the center of mass (COM) we can see the stick slip motion manifested as a variation in COM speed combinned with a side to side motion as shown in figure 1.9*a*. To increase this effect we also show the same plot with a spring ... move with spring constant 30 N/m in figure 1.9b. While the max speed is on the same scale the side to side motion is increased (notice that the axis scale is different between figure 1.9a and 1.9a).

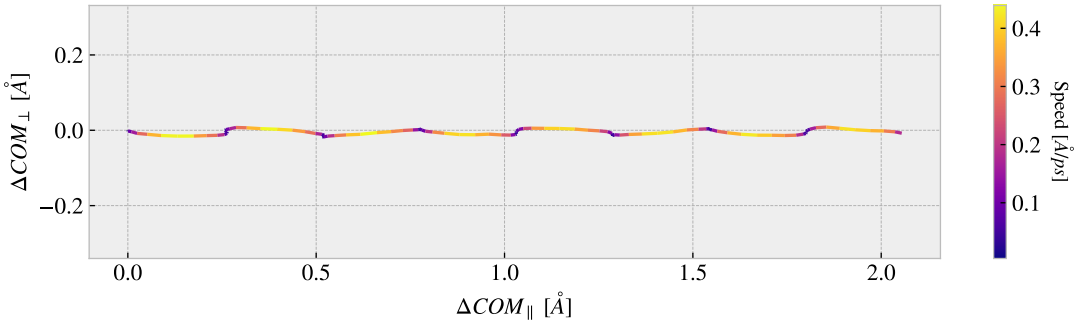

(a) Fix move

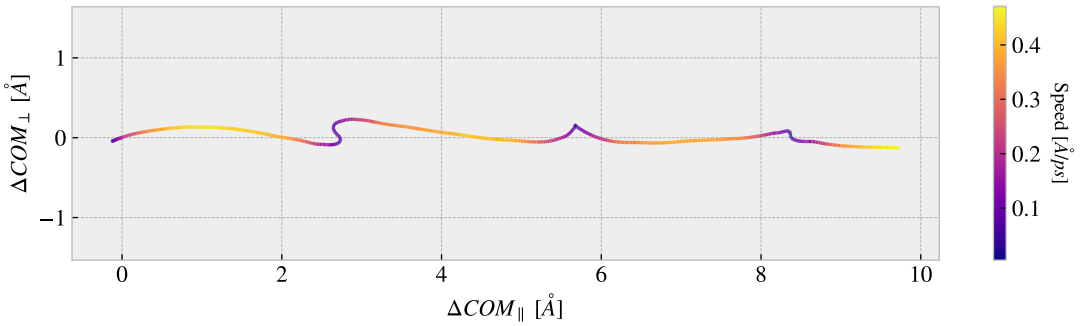

(b) K = 30

Figure 1.9: Center of mass relative position from start of drag phase in terms of axis parallel to drag direction $\Delta COM_\parallel$ and axis perpendicular to drag direction $\Delta COM_\perp$. The colorbar denotes the absolute speed of the COM.

1.5.6.2 Defining metrics for dynamic and static friction

We are interested taking the comprehensive friction force time series dataset and reducing it into single metrics describing the dynamic and static friciton respectively. The natural choice is to use the mean and max values.

Dynamic friction For the dynamic friction measurement we take the mean of the latter half of the data to ensure that the system has stabilished itself before taking the mean. For a full drag simulation of 400 Å we would thus base our mean value on the latter 200 Å drag. In figure 1.10a we have shown the friction force of the first 10 Å of drag together with a running mean with window length 50% of the corresponding data length. The final mean value estimate is indicated with red point at the end and we clearly observe that the length of sampling is insufficient since we ger a negative friction force. Nonetheless, one approach to quanity the uncertainy of the final mean estimate is to consider the running mean. The more the running mean fluctuates the more uncertainty is associated with the final estimate.

We should not care for flucations in the initial part of the running mean curve as this is still including data from the beginning, where it might transistion from static to dynamic friction. Only the running mean "close" to the ending should be considered for our uncertainty. From the Fourier analyse we concluded that longest period of any dominant oscialltions is ~ 71 Å^{-1} corresponding to $\sim 35\%$ of the running mean window of 200 Å drag. Hence we use use standard deviation of the final 35% of the running mean curve to approximate the uncertainty of the final mean value. By dividing with the final running mean we effectively calculate the relative error as shown in figure 1.10b. Naturally, we get a relative error of $\sim 257\%$ which corresponds with the mean value taking an unexpected negative value.

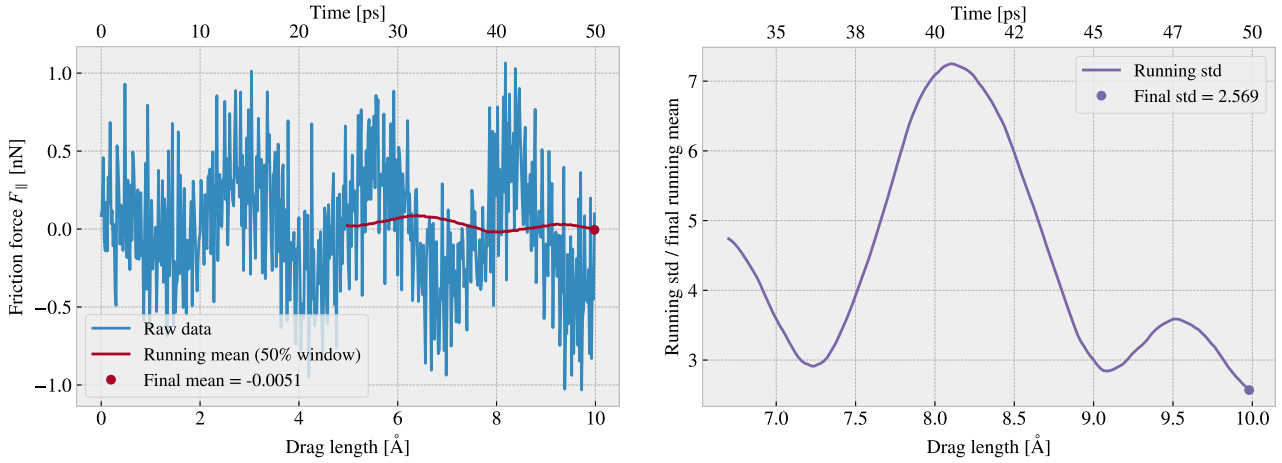

(a) Running mean

(b) Running std

Figure 1.10: Running std

When we include the full 400 Å drag, such that std window actually matches with the longest period of oscillations expected from the data, we get a final relative. error of $\sim 12\%$ as shown in fig 1.11. This is just at the limit for an acceptable error, but as we shall see later (refer to figure or something) this high error is mainly connected to the cases of low friction. When changing the simulation parameters, such that the mean friction evaluate to considerable higher values, the relative error drops to around (put in numbers). One explanation is that the osccilations in the running mean does not increase linearly with the magnitude of the friction, and hence the relative error might spike especially for the low friction cases.

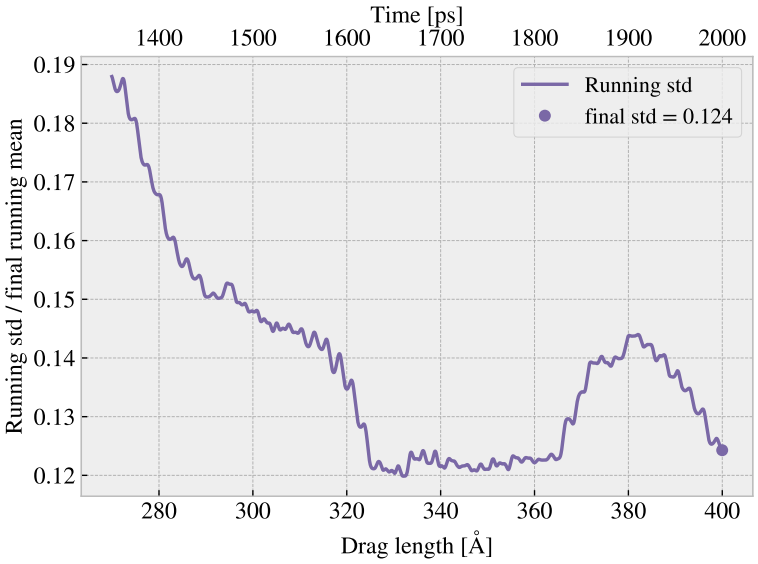

Figure 1.11: ...

Static friction The max value is the most obvious choice for adressing the static friction, even though that the definition of the static friction is a bit vague. At least when judging from the raw data in figure 1.6 we not see a textbook example of the static friction precourser (maybe include a classic static friction curve in the theory... I'm not completely sure what to expect here). Additionally the global max value does not always lie in the initial part of the simulation.
For a proper static friction evaluation we should increase force slowly and wait for the slip response. Here we drag quite fast making it diffucult to assess the static response.
We investigate the placement of the max values, i.e. the drag length for which we measure the max friction force. We show the placement of the top three max values for different simulatiosn with varying normal force in figure 1.12. We observe immediately that only a few top three max values is measured within a full slow period of ~ 71 Å. In fact many max values is measured just before the end of the simulation. This indicates that the naive approach of using the overall max value to describe the static friction coefficient might be a to naive approach. Another approach is to use the max value within a single period, but we do not really know if this period will be similar for alle cut patterns and thus this might be limiting.

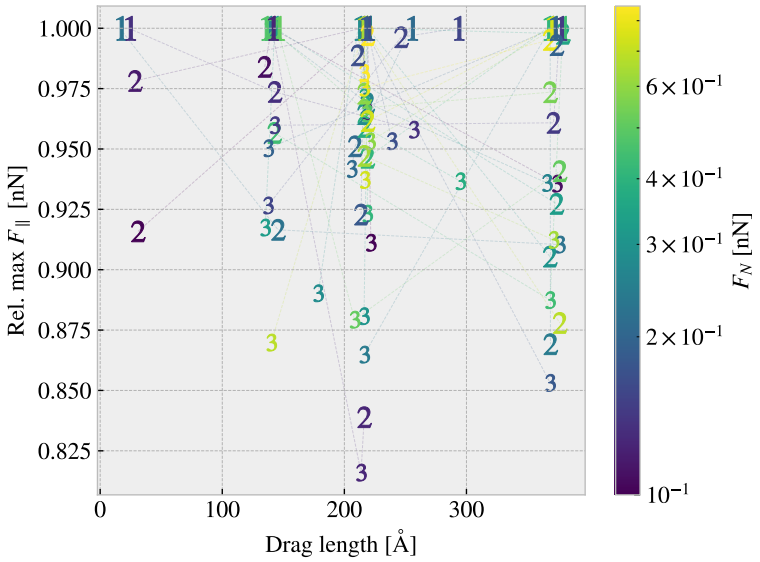

Figure 1.12: Distribution of top 3 max values for different normal force

1.5.6.3 Varying temperature, drag speed, spring constant and dt

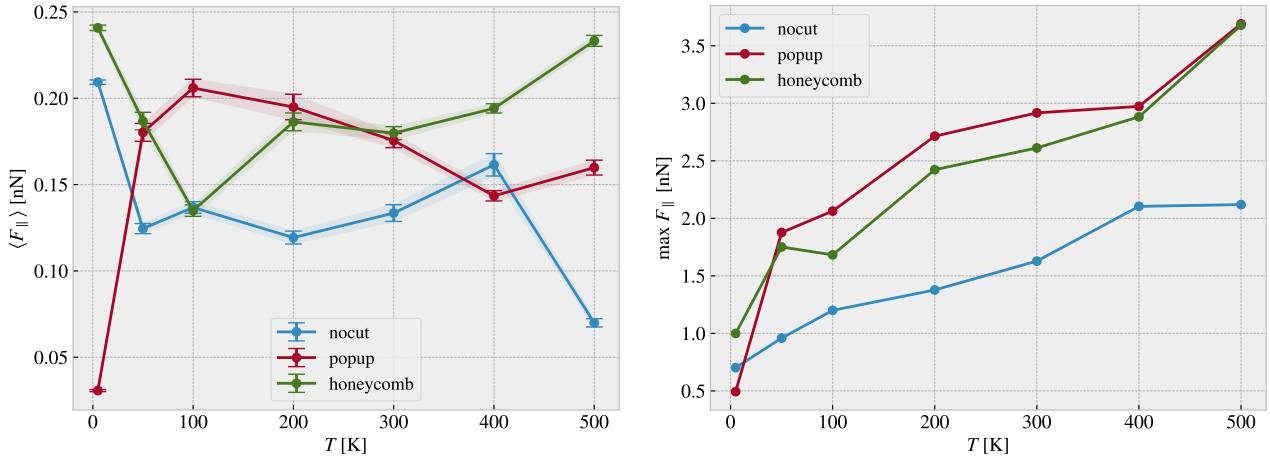

(a) mean friction **(b)** max friction

Figure 1.13: Temperature

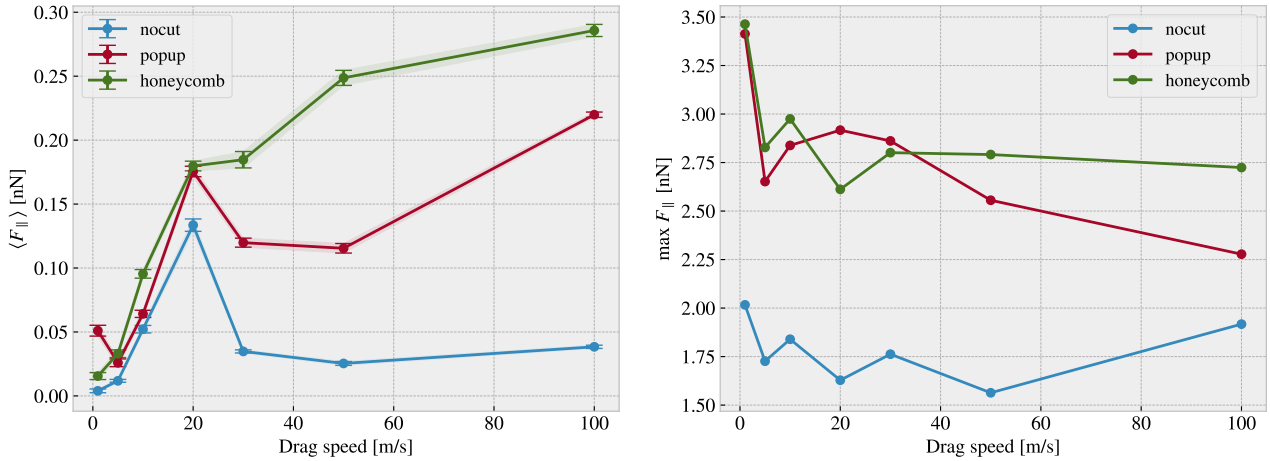

(a) mean friction **(b)** max friction

Figure 1.14: Drag speed

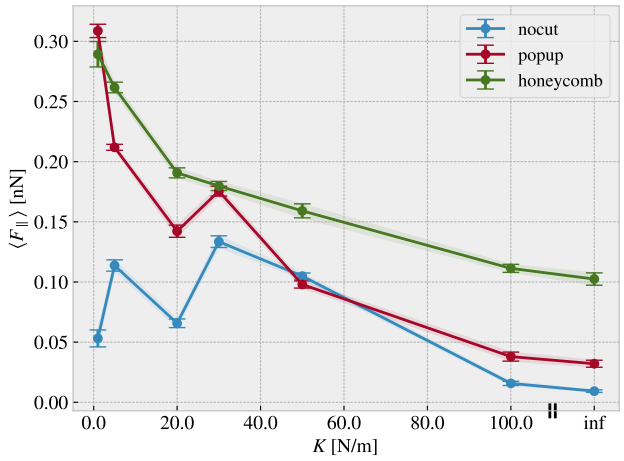

(a) mean friction

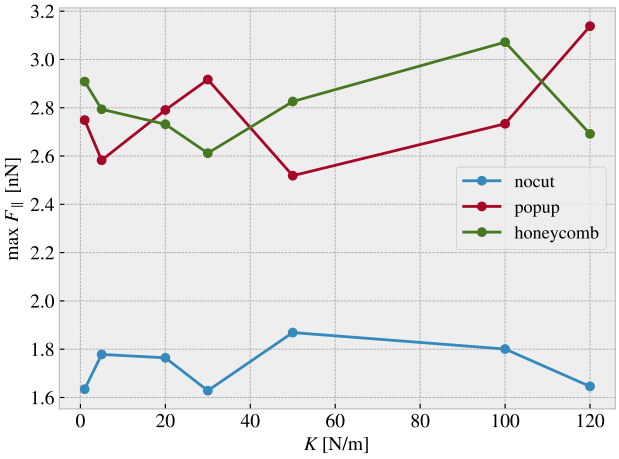

(b) max friction

Figure 1.15: Spring constant

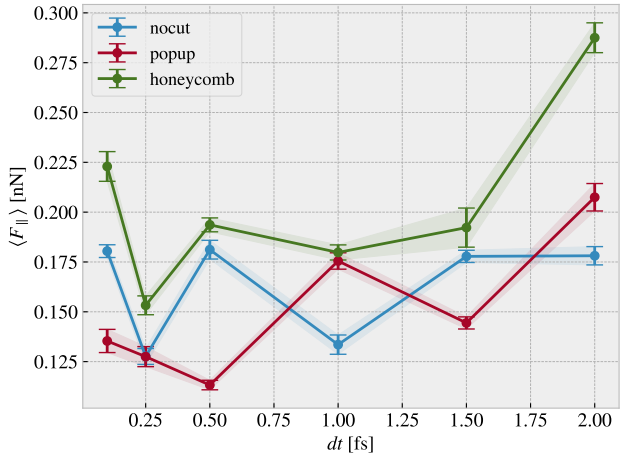

(a) mean friction

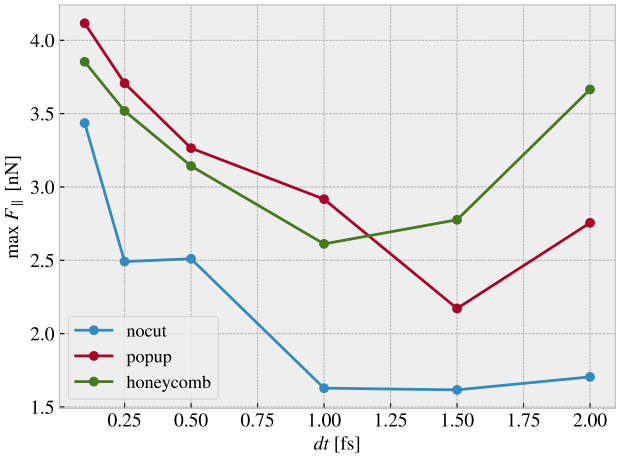

(b) max friction

Figure 1.16: Timestep

1.5.6.4 Varying normal force and stretch

Multi stretch text

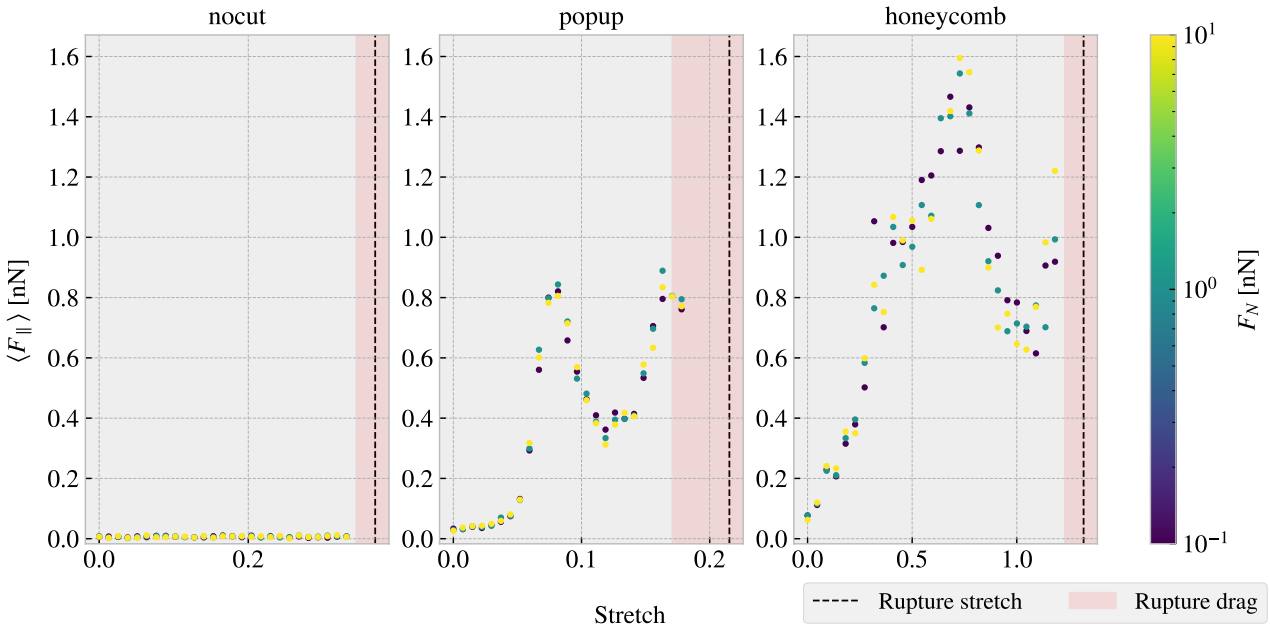

Figure 1.17: ...

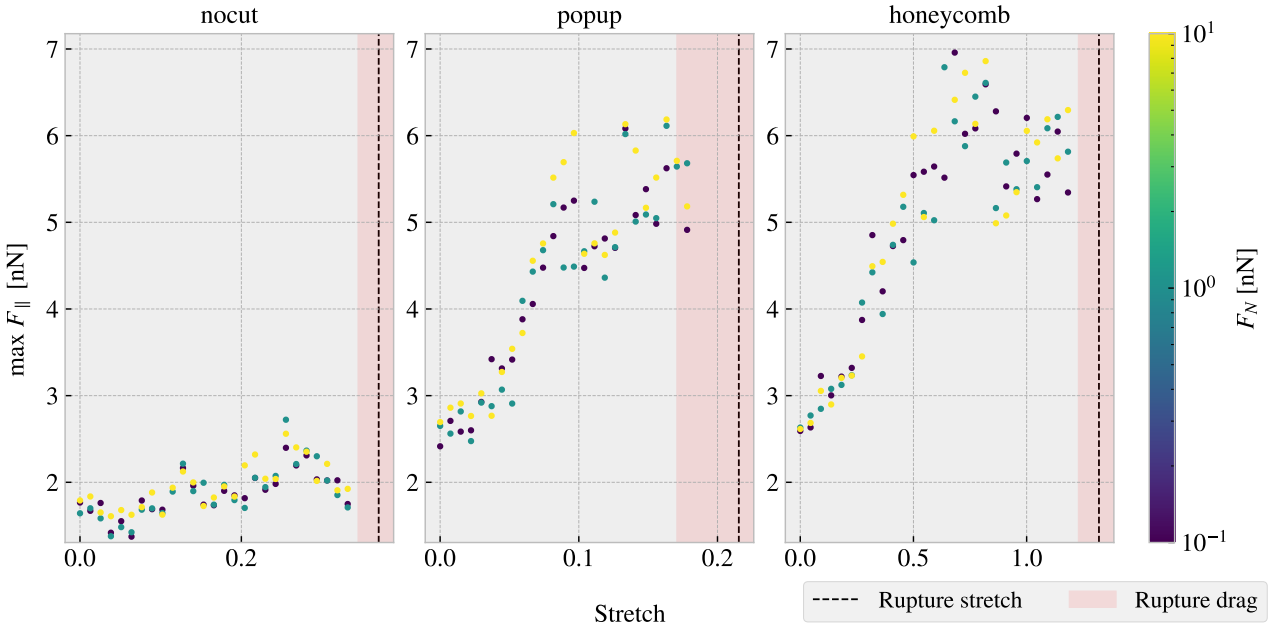

Figure 1.18: ...

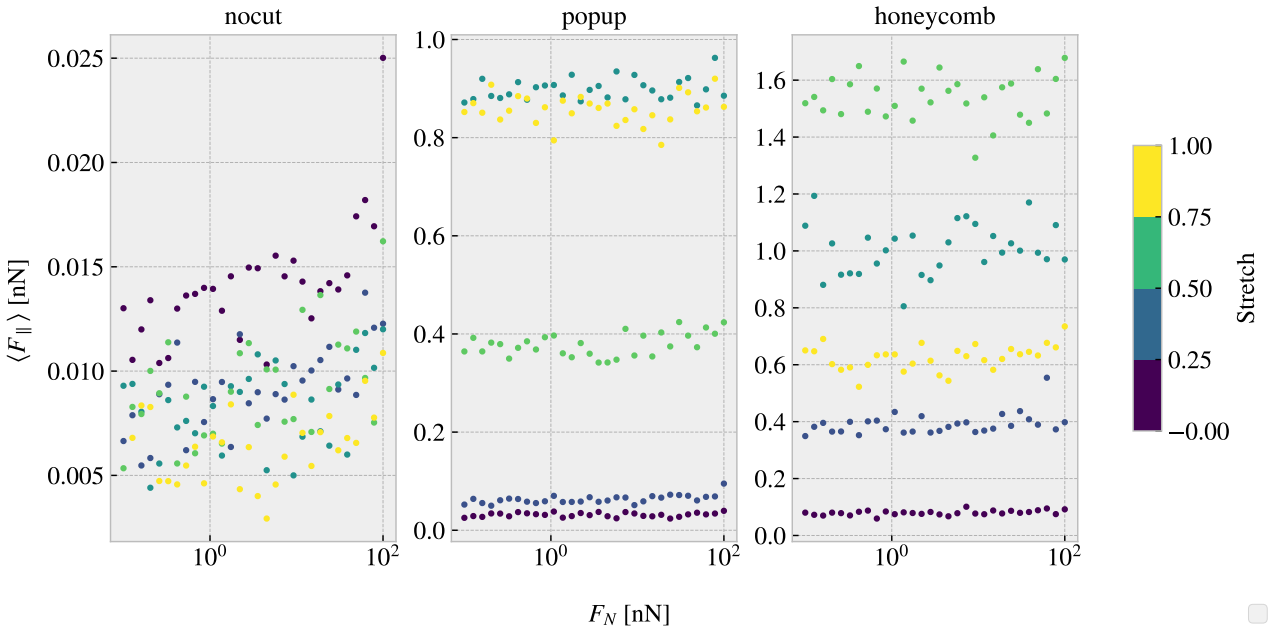

Figure 1.19: ...

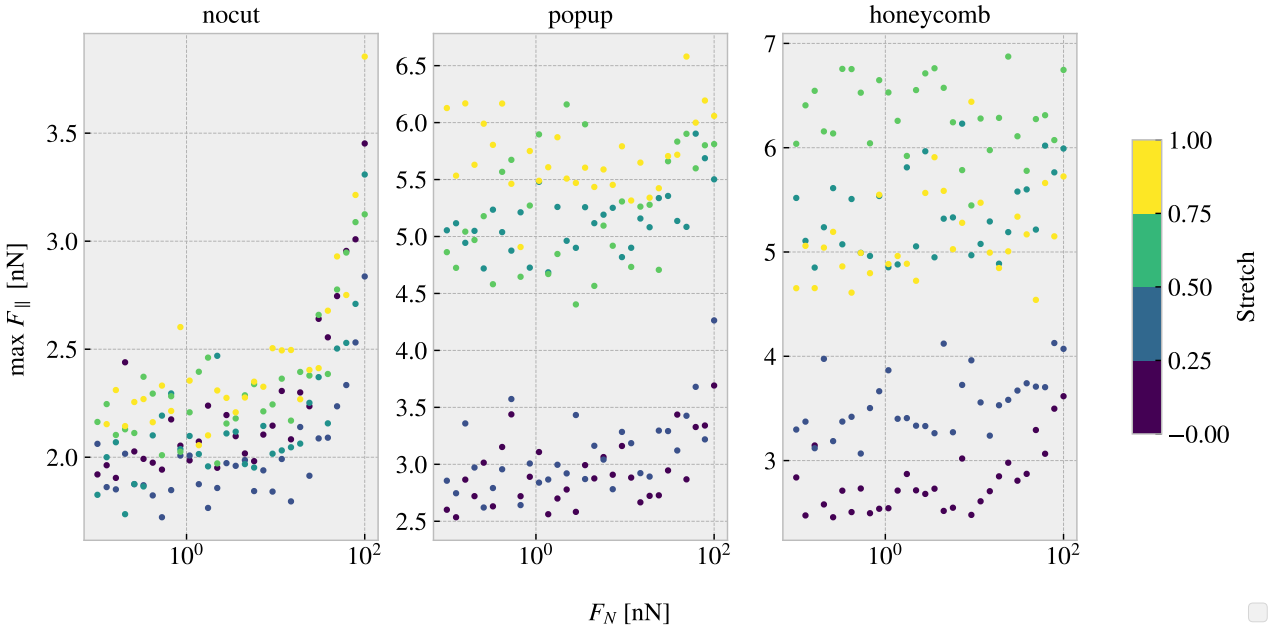

Figure 1.20: Colorbar is only fitted for the right plot (honeycomb)... this should be fixed. Should I have run a linear distribtion of FN so I could plot it linear here also...?

Table 1.5: Mean friction coeff

nocut	$0.00009 \pm 1 \times 10^{-5}$	$0.00005 \pm 1 \times 10^{-5}$	$0.00004 \pm 1 \times 10^{-5}$	$0.00005 \pm 2 \times 10^{-5}$	
popup	$0.00005 \pm 3 \times 10^{-5}$	$0.00024 \pm 5 \times 10^{-5}$	$0.0002 \pm 2 \times 10^{-4}$	$0.0005 \pm 1 \times 10^{-4}$	$0.0003 \pm 2 \times 10^{-4}$
honeycomb	$0.00013 \pm 6 \times 10^{-5}$	$0.0006 \pm 3 \times 10^{-4}$	$0.0004 \pm 6 \times 10^{-4}$	$0.0007 \pm 6 \times 10^{-4}$	$0.0009 \pm 3 \times 10^{-4}$

Table 1.6: Max friciton coeff

nocut	$0.0139 \pm 9 \times 10^{-4}$	$0.0083 \pm 7 \times 10^{-4}$	$0.010 \pm 1 \times 10^{-3}$	$0.0105 \pm 9 \times 10^{-4}$	
popup	$0.007 \pm 2 \times 10^{-3}$	$0.010 \pm 2 \times 10^{-3}$	$0.007 \pm 2 \times 10^{-3}$	$0.009 \pm 3 \times 10^{-3}$	$0.006 \pm 2 \times 10^{-3}$
honeycomb	$0.010 \pm 1 \times 10^{-3}$	$0.007 \pm 2 \times 10^{-3}$	$0.007 \pm 3 \times 10^{-3}$	$0.000 \pm 3 \times 10^{-3}$	$0.004 \pm 3 \times 10^{-3}$

Multi normal force The friction probably does not increase with normal force at an expected rate due to the fact the normal force is only applied on the pull blocks. Especially with the cutted sheet the tension drops such that the effecive normal force on the inner sheet is not changing so much. By this theory the friction force vs. normal force on the pull graph look a bit more like expected.

When looking at the graphs for the PB the max friction is visually textbook linear, while the mean friction is a bit more linear but also with negativ coefficients.

1.5.6.5 Contact area

Show plots of contact area vs stretch and discuss the fact that friction actually increases while contact area drops. Is the conclusion that there might be another more dominant cause of the increasing friction.

Bibliography

[1] E. Gnecco and E. Meyer, *Elements of Friction Theory and Nanotribology*. Cambridge University Press, 2015, 10.1017/CBO9780511795039.

[2] J. H. Dieterich, *Time-dependent friction in rocks*, *Journal of Geophysical Research (1896-1977)* **77** (1972) 3690–3697, [https://agupubs.onlinelibrary.wiley.com/doi/pdf/10.1029/JB077i020p03690].

[3] H.-J. Kim and D.-E. Kim, *Nano-scale friction: A review*, .

[4] Y. Mo, K. T. Turner and I. Szlufarska, *Friction laws at the nanoscale*, .

[5] N. Manini, G. Mistura, G. Paolicelli, E. Tosatti and A. Vanossi, *Current trends in the physics of nanoscale friction*, *Advances in Physics: X* **2** (may, 2017) 569–590.

[6] S. Li, Q. Li, R. W. Carpick, P. Gumbsch, X. Z. Liu, X. Ding et al., *The evolving quality of frictional contact with graphene*, .

[7] J. Tersoff, *New empirical approach for the structure and energy of covalent systems*, *Phys. Rev. B* **37** (Apr, 1988) 6991–7000.

[8] S. Corporation, "pair_style lj/cut command."

[9] X. Wang, S. Ramírez-Hinestrosa, J. Dobnikar and D. Frenkel, *The lennard-jones potential: when (not) to use it*, *Phys. Chem. Chem. Phys.* **22** (2020) 10624–10633.

[10] R. Naeem, "Lennard-jones potential."

[11] Q. Zhang, D. Diao and M. Kubo, *Nanoscratching of multi-layer graphene by molecular dynamics simulations*, *Tribology International* **88** (2015) 85–88.

[12] S. Corporation, "pair_style sw command."

[13] F. H. Stillinger and T. A. Weber, *Computer simulation of local order in condensed phases of silicon*, *Phys. Rev. B* **31** (Apr, 1985) 5262–5271.

[14] S. Corporation, "pair_style tersoff command."

[15] T. Schneider and E. Stoll, *Molecular-dynamics study of a three-dimensional one-component model for distortive phase transitions*, *Phys. Rev. B* **17** (Feb, 1978) 1302–1322.

[16] P. H. Hünenberger, *Thermostat Algorithms for Molecular Dynamics Simulations*, pp. 105–149. Springer Berlin Heidelberg, Berlin, Heidelberg, 2005. 10.1007/b99427.

[17] S. Corporation, "fix langevin command."